ROBOMECH Journal

RESEARCH ARTICLE

Open Access

Development and flight-test verification of two-dimensional rotational low-airspeed sensor for small helicopters

Daigo Fujiwara[1*] and Takumi Tonoike[2]

Abstract

This paper describes the development and the verification of flight test results of a differential pressure-based, two-dimensional low-airspeed sensor designed for the navigation or disturbance detection in small helicopters. The compact and lightweight sensor is integrated with the main rotor of a small helicopter and comprises two probes at both arm ends, a differential pressure sensor, rotary encoder with one magnet and two sensors, microcomputer, a wireless data link, and battery. It measures the differential pressure between the total pressures captured by two total-pressure probes at each rotor angle, instead of using static pressure probes. Thus, the airspeed of the fuselage can be evaluated from the low speed. Flight tests were conducted employing a reference ultrasonic two-dimensional airspeed sensor for comparison. The results demonstrated that the magnitude error of the airspeed is less than 2 m/s for low-airspeed flights (<∼23 m/s) when utilizing Pitot-type probes. The error in wind angle approximated 30°, and the delay was less than or equal to that observed with a global navigation satellite system sensor.

Keywords Low-airspeed sensor, Navigation, Small helicopter, Flight test

Introduction

Small unmanned helicopters are applied in various roles including fixed-point observation and cargo transportation, benefiting from capabilities such as vertical take-off and landing, hovering, and low-speed cruise. These aircraft are susceptible to atmospheric disturbances, necessitating airspeed measurement techniques that suppress these disturbances and improve the control performance. Generally, the airspeed of a helicopter during low-speed flight is typically lower than that of a fixed-wing aircraft, with a significant angle difference between the airspeed vector and the fuselage station axis.

*Correspondence:
Daigo Fujiwara
daigo_fujiwara@faculty.chiba-u.jp
[1] Graduate School of Engineering, Chiba University, 1-33, Yayoi-cho, Inage-ku, Chiba 2638522, Japan
[2] Faculty of Engineering, Chiba University, 1-33, Yayoi-cho, Inage-ku, Chiba 2638522, Japan

Various types of airspeed sensors are employed on aerial vehicles. For fixed-wing aircraft, Pitot tubes are commonly utilized to determine velocity from the differential between total and static pressures. Multi-hole Pitot tubes can measure the angles of attack and side-slip, in addition to velocity magnitude. An instance of a five-hole tube is presented in [1]. Alternatively, a method employing the pressure on airframe skin holes for airspeed calculation is documented in [2]. Rotary-wing aircrafts encounter numerous challenges that prompt the development and evaluation of various methodologies. The first prevalent technique involved the ultrasonic wave method, where a speaker and microphone were positioned opposite each other, calculating wind speed by measuring the time or phase of the ultrasonic wave. A study in [3] detailed the flight test evaluation of a three-dimensional ultrasonic-wave-based airspeed sensor mounted at the fuselage front, displaying satisfactory airspeed accuracy except during backward flight. Kawahara et al. [4] introduced a handmade, lightweight, small-sized three-dimensional

ultrasonic sensor designed for unmanned aerial vehicles. With the advent of commercial off-the-shelf sensors [5], two-dimensional sensors have been adopted for weather observation via multirotor vehicles in [6]. Although three-dimensional sensors are generally large, instances of onboard applications have been documented [7]. The second method employs pressure measurements for airspeed and direction determination. Hrishikeshavan et al. [8] developed cross-shaped multi-hole pressure probes along with pressure holes on the wing skin to determine forward and vertical velocities and the angle of attack, facilitating stall detection during the transition from hover to level flight. Yeo et al. [9] designed custom-built triaxial symmetric pressure probes for identifying other aerial vehicles by sensing downwash, enabling disturbance-free trajectory planning and flight speed measurement. Haneda et al. [10] introduced a spherical probe with pressure holes distributed along the cross-section of a spherical surface. This design incorporates three sets of MEMS pressure sensors to measure differential pressures across opposite holes, with two-dimensional airspeed and direction deduced through a deep neural network model. Although wind tunnel tests confirmed the high accuracy of the model, detailed evaluations by flight tests have not yet been conducted. Zhao et al. [11] developed a cylindrical probe (30 mm in diameter and 80 mm in length) equipped with pressure holes on its surface to compute two-dimensional airspeed and direction using differential pressure measurements. Wind tunnel tests validated the accuracy, though outdoor flight tests revealed notable discrepancies when compared with data from weather observation towers. The third methodology integrates pressure sensors with vanes and swivels. A sensor of this type, as described in [12], was mounted on the front of a large helicopter. Additionally, a brochure [13] details a military-use swiveling sensor, while Kaletka [14] assesses the accuracy of a device affixed to the fuselage. Similar products are highlighted in brochures [15]. The fourth strategy focuses on flow detection in which heat sources and temperature sensors gauge airflow from temperature distribution, subsequently converting this data into airspeed readings. Bruschi et al. [16][17][18] proposed a two-dimensional airspeed sensor that utilizes airflow impacting and passing through unique microchannel structures etched into a poly methylmethacrylate vertical cylinder, connected to flow sensors. This concept is envisioned for implementation as a mobile anemometer on a multirotor vehicle. Wang et al. [19] measured the three-axis airspeed in a multirotor vehicle by orthogonally positioning three single-axis flow meters. Moreover, Abichandani et al. [20] mentioned the airspeed estimation by using the mathematical model and attitude angles of an aircraft, measured by an inertial measurement unit (IMU) and global positioning system (GPS), categorizing it broadly as an airspeed measurement technique. Duncan [21] provided an overview of the performance requirements for an air-data sensor (ADS) in helicopters, describing the merits and limitations of nine low airspeed sensing methods, including the methods described earlier. He advocated against the direct application of the Pitot concept; conversely, he identified the rotational method as the most sophisticated, which closely aligns with the set criteria. At low airspeeds, where measurement is exerted through pressure methods using differential pressure sensors like Pitot tubes, the signal-to-noise ratio deteriorates significantly due to the quadratic relationship between pressure and speed. The rotational approach employs two pressure probes attached to the extremities of a rotating arm, calculating the two-dimensional airspeed along the rotor plane by assessing the differential pressure between these probes. Daw [22] suggested the placement of two probes beneath the tip of a rotor blade, converting the pressure into an electrical signal transmitted to the fuselage via a coil, where the airspeed is subsequently decoded. Slabinski et al. [23] designed probes for rotor blades, whereas Abbott, Onksen, et al. [24][25] introduced a specialized arm unit that can rotate at a constant rate above the main rotor of the helicopter to detect the differential pressure between two edge-mounted probes. This pressure data is relayed to the air-data computer (ADC) on the body of the helicopter through the hollow main rotor shaft, which enables the ADC to compute the two-dimensional airspeed. Actual manned helicopters have adopted several instances of this technology. The rotational-type sensor offers several advantages: (1) airspeed correlates directly with differential pressure, ensuring a robust signal-to-noise ratio across a wide speed range; (2) its proximity to the rotor enhances its utility; and (3) it exhibits a rapid response time compared to the vane or swivel type; (4) no obstacles are present that could diminish airflow surrounding the probe, unlike the ultrasonic type, and (5) the rare occurrence of pipe clogging is a potential issue with flow detection types. Nonetheless, the primary disadvantage of traditional rotational-type sensors lies in their complex structure, specifically: (1) The placement of the probe on the rotor requires intricate piping to the ADC on the fuselage. (2) The presence of moving mechanical components, driven by a dedicated motor owing to the low main-rotor speed in large manned helicopters, requires hardware modifications for small helicopters owing to space constraints and wiring requirements.

This research introduces a novel rotational low-airspeed sensor designed for navigation and atmospheric disturbance detection in small unmanned single-rotor

helicopters and evaluated its performance. Based on the methodologies explained in previous studies [24, 25], this design compactly integrates all critical components, i.e., probes, pressure sensors, magnetometers for rotor-angle sensing, air-data computers, wireless data links, and batteries, above the main rotor. The limitations of the installation position of the sensor were relaxed because the upper (above-the-rotor) part was structurally separated from the lower (fuselage side) part, thereby eliminating the wires passing through the cylindrical main shaft. Unlike earlier designs requiring a dedicated motor due to the slow speed of the large main rotor, the arm of this sensor is directly affixed to the main rotor, dispensing with the motor owing to the higher rotational speed of small helicopters. Previous iterations utilized cylindrical static pressure probes, but flight test results revealed inadequate airflow and differential static pressure at the high rotation speeds of small helicopters. Consequently, the probes were updated to Pitot-type or cylindrical total pressure probes, ensuring accuracy comparable to that of earlier designs [24], regardless of the simplified structure of the sensor. The accuracy of the developed sensor was assessed by comparing with a two-dimensional ultrasonic airspeed sensor and a global navigation satellite system (GNSS) sensor under various conditions, including probe types, rotor speeds, and flight velocities. This comparative analysis confirmed that the accuracy of the developed sensor aligns with that of the methodology detailed in [24]. Moreover, the minimal delay does not impair the flight control performance.

The innovation and superiority of the proposed method offer multiple advantages over traditional rotational sensors. Furthermore, the method distinguishes itself from earlier studies employing non-rotational techniques through its proven accuracy and dynamic response, which are validated via flight tests in actual outdoor settings across a broad speed range, from below 5 m/s to over 20 m/s. For instance, in [9], the flight test data were solely compared with ground speeds within a narrow ±2 m/s speed band. The study in [10] limited its speed range to within ±10 m/s, lacking comprehensive verification through flight tests. In [11], outdoor flight tests using a multirotor vehicle exhibited significant errors at low speeds compared to measurements from a weather observation tower. In [18], the flight tests on a multirotor vehicle did not present the verification data for speeds below 6 m/s. In [19], flight tests were conducted with a multi-rotor vehicle and motion capture sensors, comparing airspeed solely to ground speed within a constrained ±3 m/s speed range.

This study introduces a method for developing a low-airspeed sensor applicable to meteorological observations as well as the guidance, navigation, and control of small unmanned helicopters, with installation feasible above the main rotor. Furthermore, it provides outdoor flight experimental data that facilitate the validation of the accuracy and delay of the sensor across a broad velocity range. The experimental setup included the developed sensor, a reference airspeed sensor, and a GNSS receiver, all mounted on a small helicopter.

The hardware and software components of the developed sensor are presented in Section 2, detailing the measurement principle and the methodology for calculating airspeed magnitude and direction. The flight test conditions and procedures are listed in Section 3. The results of these flight tests are discussed in Section 4, where the accuracies of the magnitude and direction of the airspeed are confirmed through comparison with a reference airspeed sensor, and the delay is evaluated against a GNSS receiver. Lastly, the findings are summarized in Section 5.

Developed hardware and software

Small unmanned helicopter as a platform

An overview of the small unmanned helicopter equipped with both the developed and reference airspeed sensors is depicted in Fig. 1. The helicopter, an Impaction E12S by Quest Corporation, served as the platform for the flight experiments. The main rotor rotates clockwise when viewed from above, with a gross mass of 6.71 kg and a fuselage dry mass of 5.44 kg, excluding the airspeed sensors. The radii of the main and tail rotors are 0.846 m and 0.142 m, respectively. For clarity, an orthogonal coordinate system B, affixed to the fuselage, is defined as x_B, y_B, and z_B axes pointing forward, right, and downward, respectively, with the origin at the center of gravity of the fuselage.

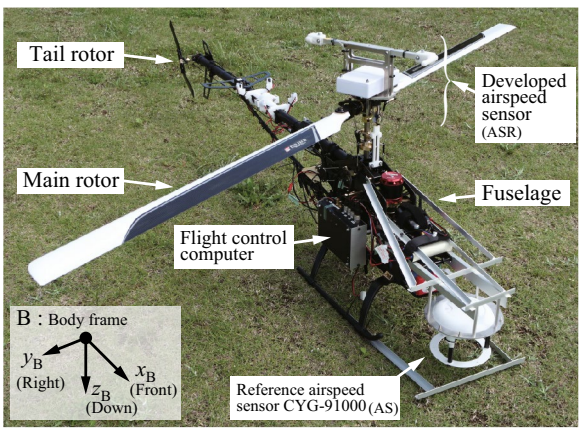

Fig. 1 Overall view of the experimental small helicopter and airspeed sensors

A two-dimensional ultrasonic anemometer (CYG-91000, R. M. Young) was used as a reference airspeed sensor and strategically positioned at the lower and front sections of the fuselage to align as closely as possible with the center of gravity. This arrangement aims to prevent the fuselage from obstructing the airflow and reduce the downwash impact from the main rotor, ensuring that the sensor head is directed downward and can accurately measure the two-dimensional airspeed along the (x_B, y_B) plane. The center of the sensor is situated 0.375 m ahead and 0.360 m below the center of the main rotor. The specifications of the reference sensor include a speed range from 0 to 70 m/s, a resolution of 0.01 m/s, an accuracy of ±2% or 0.3 m/s for speeds below 30 m/s, and a response time of 0.25 s, with a measurement sampling time preset at 0.1 s. This sensor was calibrated via wind-tunnel tests prior to its use.

Developed low-airspeed rotational sensor

Figure 2 illustrates the overall schematic of the developed rotational low-airspeed sensor, weighing a total of 600 g. An arm equipped with probes is affixed on top of the stay assembled from A5052 aluminum plate, which is consequently attached to the main rotor hub. Each probe is designed with a pressure measurement hole; the setup includes both total and static pressure probes. The total pressure probe is oriented such that its hole faces the direction of travel, whereas the static pressure probe features a hole on its side surface relative to the direction of travel. This hole is located 0.115 m above the main rotor plane and 0.150 m radially from the rotation center. The pressure captured by these probes is relayed to a differential pressure sensor via connecting tubes. Additionally, two magnetometers are mounted on the underside of the stay facing downward detect the passage of a magnet affixed to the front side of the fuselage.

Three distinct types of probes were fabricated. The first, a pitot-type probe, depicted in Figs. 2a and 3a, measures the total pressure. The second, a cylindrical probe illustrated in Fig. 3(b), also assesses the total pressure, representing the approach in references [24][25] but with a focus on total rather than static pressure measurement. The third, termed a cylindrical static pressure probe and shown in Fig. 3c, features a side-mounted hole on the cylindrical surface for static pressure measurement. Each probe is crafted through 3D printing and finished manually to ensure a smooth surface.

Figure 4 displays the circuit box, housing differential pressure sensors, a microcomputer, a wireless data link, a battery, and weights for center of gravity adjustment. A differential pressure sensor (HSCDRRN010NDAA3, Honeywell) detected a differential pressure range of ±2491 Pa and outputted pressure recordings as an analog voltage. Its accuracy stands at ±0.25%FSS, with a resolution of 0.03%FSS, and a response time of 1 ms. Although two differential pressure sensors are installed for mass balance, and only one is actively used, with tubes from the probes connected to this single sensor. The microcomputer (PIC32MZ2048EFM064, Microchip) incorporates peripheral functions such as 12-bit A/D converters and input capture modules. A wireless data link (XBee S2C, Digi International) was utilized, and the battery specification included a Li-Fe, 2-cell, 550 mAh capacity.

Figure 5 illustrates the signal flow and processing mechanism. Pressure from the probes, located at each arm end, is transmitted through pressure tubes to the

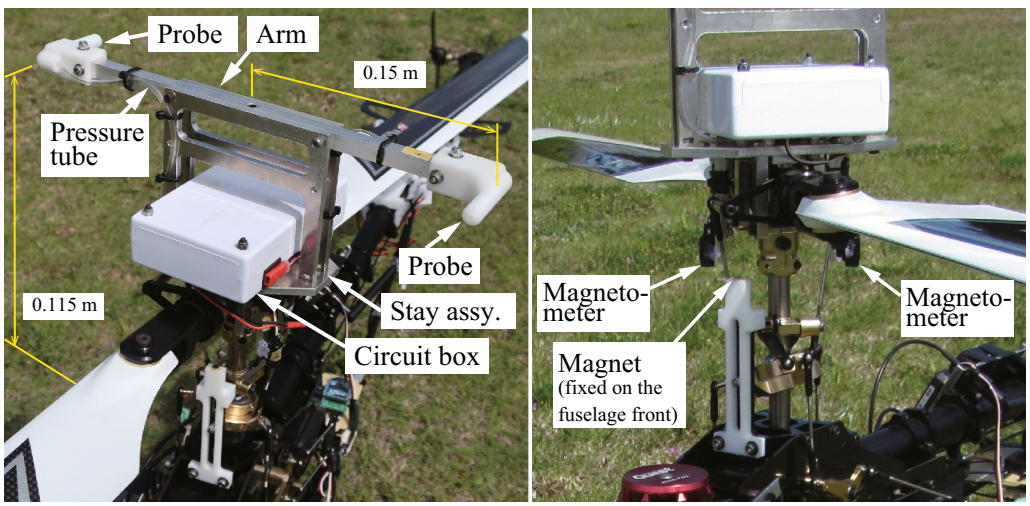

Fig. 2 Magnified views of **a** upper rotational part and **b** lower rotational part of the developed low-airspeed sensor

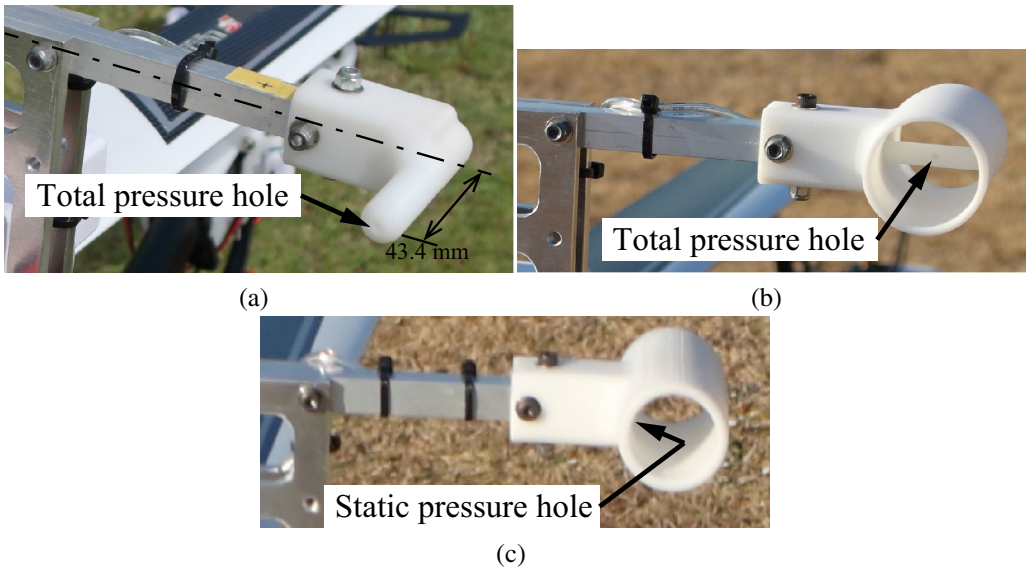

Fig. 3 Magnified view of the probes; **a** Pitot-type (total-pressure) probe (P1), **b** Cylindrical (total-pressure) probe (P2), and **c** Cylindrical static-pressure probe

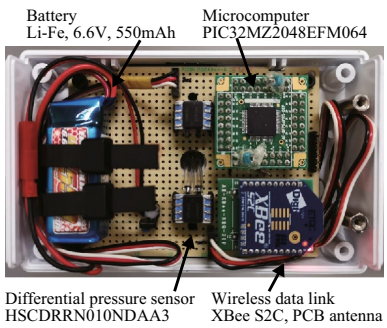

Fig. 4 Interior of the circuit box

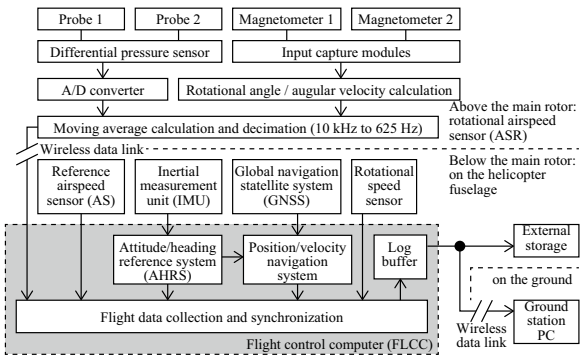

Fig. 5 Signal flow diagram about the developed sensor and other flight control/measurement devices

differential pressure sensor within the circuit box. This sensor is equipped with two pressure ports, which identifies the differential pressure across the pressure holes of the probes. The output of the sensor is digitized via a 12-bit A/D converter and relayed to the microcomputer. When the magnet crosses the sensor tip, each magnetometer generates a high voltage signal, switching to a low voltage at other intervals. The input capture module of the microcomputer precisely logs the transit time of the magnet based on the pulse-voltage data, which aids in the calculation of the rotational speed and angle of the main rotor. This information along with the differential pressure data is periodically forwarded to the flight control computer on the helicopter fuselage through a wireless data link. The voltage of the differential pressure sensor is converted to digital data at a sampling rate of 0.1 ms (10 kHz). Owing to the throughput constraints of the wireless data link, a moving average of 10 samples is computed, which subsequently reduces the data to a frequency of 1.6 ms. Every 10 ms, six pieces of data are transmitted to the flight control computer. For instance, at a rotational speed of 151.8 rad/s (1450 min^{-1}), the main rotor advances approximately 14° in 1.6 ms. The flight control computer consolidates data from the navigation system, including IMU and GNSS data, the reference airspeed sensor, and the rotational airspeed sensor, into a log buffer. This log data is stored in nonvolatile memory and partially transmitted to a ground station PC. In this study, a flight control computer was used for only

collecting and recording the data and not for controlling the helicopter.

The differences between the conventional sensors [24] [25] designed for large helicopters and the proposed sensor are discussed herein. In conventional sensor configurations, a dedicated motor is required to rotate the arm due to the low rotational speed of the main rotor. Furthermore, wires must traverse the hollow main rotor shaft to establish a connection between the rotating component and the ADC on the fuselage side, with rotor-angle measurement and signal processing executed by the ADC. Conversely, the sensor developed herein integrates the arm, probes, differential pressure sensor, and power supply with the main rotor into a cohesive unit that rotates in sync with the main rotor. At the fuselage side, the only component required is a magnet. Wireless communication on the fuselage eliminates the need for complex structures such as hollow main rotor shafts and rotary joints, thereby simplifying installation on small helicopters with limited space and payload capacity. With the microcomputer positioned on the rotor, the process spanning from pressure measurement to advanced signal processing is consolidated within the rotor-side unit, enhancing efficiency. Moreover, traditional methods typically utilize the static pressure difference based on the Venturi tube principle, whereas the approach presented here leverages the total pressure difference. As described in the following section, the change in differential pressure relative to the change in airspeed was small when using static pressure probes and relatively large when using total pressure probes. Therefore, total pressure probes were adopted by the proposed method.

Measurement theory and the method of calculation

The measurement principle of the rotational speed sensor is illustrated in Fig. 6. Assuming that a uniform wind with a velocity of V_{Wp} is perpendicular to the longer direction of the arm, and the sensor arm (with a radius of L) is rotating at an angular velocity of Ω. As probe No. 1 is in the tailwind, airspeeds V_1 of probe 1 and V_2 of probe 2 can be expressed as follows: V_Ω denotes the linear velocity at the probe generated by the rotation.

$$V_1 = V_\Omega - V_{\mathrm{Wp}} \tag{1}$$

$$V_2 = V_\Omega + V_{\mathrm{Wp}} \tag{2}$$

$$V_\Omega = 2\pi\Omega L \tag{3}$$

Let P_{t1} and P_{s1} denote the total and static pressures at the probe 1, P_{t2} and P_{s2} indicate the total and static pressures at the probe 2, respectively, and ρ represent the air density. The Bernoulli equation is expressed as follows:

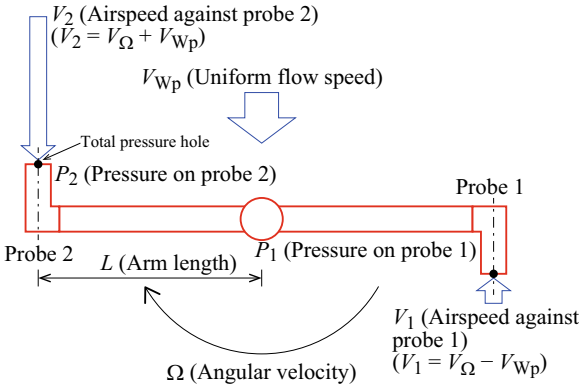

Fig. 6 Illustration of the airspeed measurement mechanism

$$\frac{1}{2}\rho V_1^2 + P_{\mathrm{s1}} = P_{\mathrm{t1}} \tag{4}$$

$$\frac{1}{2}\rho V_2^2 + P_{\mathrm{s2}} = P_{\mathrm{t2}} \tag{5}$$

Subtracting Equation (4) from Equation (5) and arranging it using total pressure difference $\Delta P_{\mathrm{t}} = P_{\mathrm{t2}} - P_{\mathrm{t1}}$ and static pressure difference $\Delta P_{\mathrm{s}} = P_{\mathrm{s2}} - P_{\mathrm{s1}}$,

$$\frac{1}{2}\rho(V_2^2 - V_1^2) = \Delta P_{\mathrm{t}} - \Delta P_{\mathrm{s}} \tag{6}$$

By substituting Eqs. (1) and (2) into Eq. (6), the magnitude of the wind speed V_{Wp} can be obtained using the following equation:

$$V_{\mathrm{Wp}} = \frac{\Delta P_{\mathrm{t}} - \Delta P_{\mathrm{s}}}{2\rho V_\Omega} \tag{7}$$

Airspeed calculation method about the developed rotational sensor

First, the symbols in Fig. 7 are defined as follows: V_{W} denotes the magnitude of the uniform wind. The direction of the uniform wind, ψ_{W}, is represented by the angle of the upstream direction measured clockwise from the x_{B} axis observed from above. ψ_{RP} indicates the arm angle measured clockwise from the center of rotor with respect to the $-y_{\mathrm{B}}$ axis direction. ψ_{RM} denotes the angle of the magnetometer 1 clockwise from the x_{B} axis. As the angle between Magnetometers 1 and 2 is 20°, the following relationship can be obtained: $\psi_{\mathrm{RP}} = \psi_{\mathrm{RM}} - 110 \times \pi/180$ rad. (or $\psi_{\mathrm{RP}} = \psi_{\mathrm{RM}} + 250 \times \pi/180$.)

Subsequently, the procedure of deriving V_{W} and ψ_{W} is explained. As the arm and probes rotate with the main rotor, the differential pressure is expected to fluctuate periodically with the rotation angle of the main rotor, provided the wind velocity V_{W} and ψ_{W} are constant.

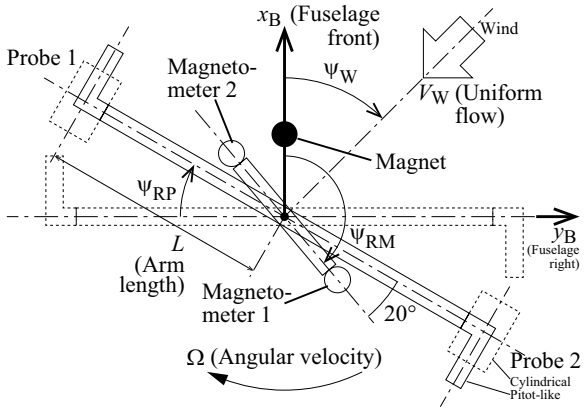

Fig. 7 Relationship of the sensor arm angle and the uniform flow direction

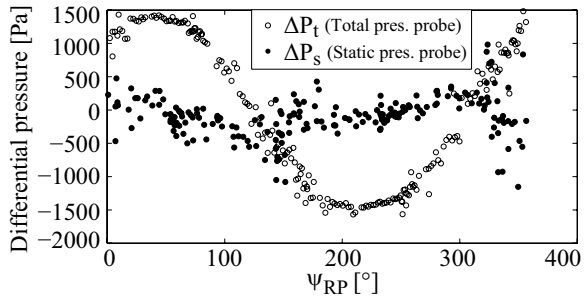

Fig. 8 Differential pressure comparison between the total pressure and static pressure probes (20 m/s, 162.3 rad/s)

Figure 8 illustrates the correlation between the measured differential pressure and the rotor angle (ψ_{RP}) during forward cruising at approximately 20 m/s, utilizing both Pitot-type total pressure probes and cylindrical static pressure probes. The total pressure difference (ΔP_t) exhibits a sinusoidal variation. Conversely, no significant relationship exists between the static pressure difference (ΔP_s) and ψ_{RP}. Thus, static pressure probes were not used, and ΔP_s is assumed to be 0 and ignored hereafter.

For a dataset comprising 50 samples (equivalent to roughly two rotor rotations) of total pressure difference (ΔP_t) and magnetometer angle (ψ_{RM}) collected from a specific moment t, the MATLAB function fminsearch() is applied to align a cosine curve with the data, aiming to minimize the sum of squared errors. This process yields the amplitude (ΔP_{amp}) and phase ($\Delta\psi$). For instance, Fig. 9(a) displays the time-series data for ΔP_t and ψ_{RM} during forward flight at an airspeed of approximately 10 m/s. Figure 9b presents the data alongside the fitted cosine curve. V_W at time t is described as V_{Wp} when ΔP_{amp} is substituted for ΔP_t in Equation (7):

$$V_W = \frac{\Delta P_{amp}}{2\rho V_\Omega} \tag{8}$$

ψ_W at time t is obtained by the following equation.

$$\psi_W = \Delta\psi - 110 \times \pi/180 \tag{9}$$

Such calculations are repeatedly conducted throughout the entire duration, incrementally shifting the sampling points, thereby the magnitude and direction of the airspeed are obtained at all instances.

To determine air density (ρ), it is essential to measure the atmospheric temperature and pressure. In this study, given that the flight occurs within the confines of the flight test field, air density values are derived from the weather meter readings available at the field.

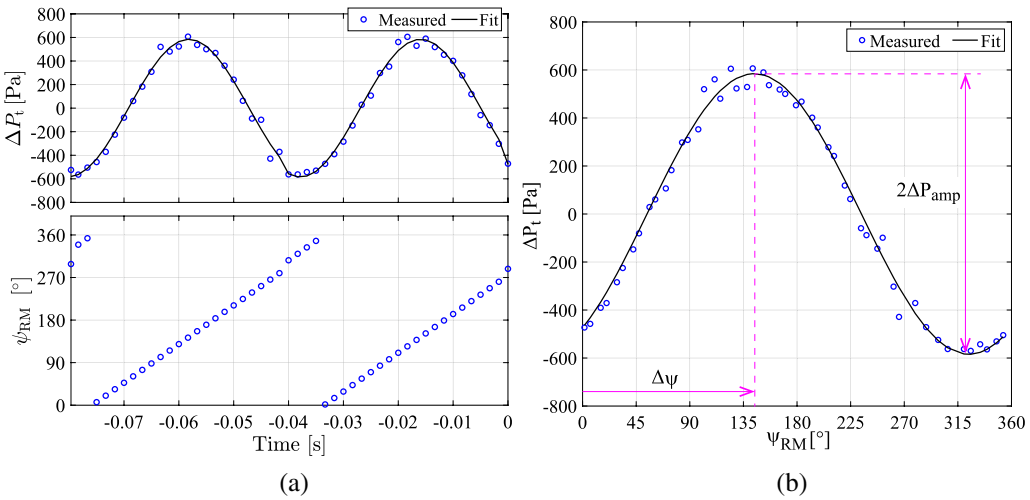

Fig. 9 Example of measured differential total pressures and the cosine curve fitted to them during cruise at about 10 m/s; **a** Time history, **b** Pressure vs sensor angle

Flight test conditions and procedures

Conditions of experiments

The objective of the flight tests was to gather data instrumental in evaluating the accuracy of airspeed magnitude, direction, and time delay under various probe conditions, rotational speeds, and horizontal flight velocities. The experimental setups are detailed in Table 1, whereas the significance of P and R is indicated in Table 2, including their subsequent numerals. The flight speed conditions were predetermined at five levels (0, 3, 8, 17, and 22 m/s), with an exclusive condition of 28 m/s for P1R1. Nonetheless, owing to the ground speed being manually aligned in most instances, the actual flight airspeeds diverged from the pre-established conditions. Consequently, the flight speed values denoted by V represent not the predefined settings but the average speeds recorded by the reference airspeed sensor.

Procedures of experiments

The experimental procedures are executed as follows: Suitable probes were attached to the arm for each test condition, and the reference rotational speed was determined using the CGY750 rotational speed governor by Futaba Corporation. Subsequently, the helicopter was launched and manually controlled. The flight maintained an altitude of approximately 10 m, with the nose of the helicopter oriented into the wind to mitigate the effects of the fuselage and downwash on the reference airspeed sensor. An observer, separate from the pilot, announced the ground speed readings from the GNSS, which guided the pilot to adjust the speed of the helicopter to match the predetermined target. The duration of hovering flights was around 30 s. For other flight modes, the constraints of the test field meant the helicopter traversed forward approximately 100 m in a single direction, including both acceleration and deceleration phases.

An analysis of test data such as the main rotor angle and total pressure difference acquired from flight tests, including airspeed calculations is conducted offline following the download of data recorded in the non-volatile memory of the flight control computer. The computation of airspeed magnitude and direction for a single sampling period utilizes an Intel Core i5-12500 CPU (with a turbo-boost clock frequency of 4.6 GHz) and a single-threaded algorithm, requiring 1.18 ms. Given that the clock frequency of the circuit box CPU is 1/23 times slower, the expected duration for online computation is ~27.1 ms. This duration is shorter than the 50 ms output interval of position and velocity data from the GNSS receiver, indicating that the computational load is sufficiently low to enable online calculation.

Table 2 Definitions of symbols for probes and reference rotational speeds

Symbol	Probe (Total-pressure)	Symbol	Speed [rad/s] ([min^{-1}])
P1	Pitot-type	R1	151.8 (1450)
P2	Cylindrical	R2	162.3 (1550)

Experimental results and performance verifications

Airspeed magnitude and angle

Tables 3, 4, 5, 6 present the average values and errors of airspeed magnitude (V_W) and direction (ψ_W) for each test scenario. ASR denotes the developed rotational airspeed sensor, whereas AS refers to the reference airspeed sensor. The error is quantified as the root-mean-square (RMS) of the differences in mean values between the rotational and reference airspeed sensors, with the V_W error also expressed as a percentage relative to the speed of the reference airspeed sensor. Figures 10, 11, 12 display the error values listed in Tables 3, 4, 5, 6, showcasing the numerical error data. Figures 13, 14, 15, 16 depict the time-history responses derived from the test data used to compute the values in Tables 3, 4, 5, 6. In these figures, the solid line (ASR) illustrates the response of the developed rotational airspeed sensor, the dashed line (AS) indicates the response of the reference airspeed sensor,

Table 1 Test cases (Number after V is a velocity measured by the reference airspeed sensor)

No.	Symbol	No.	Symbol	No.	Symbol	No.	Symbol
1	P1R1V1.4	8	P1R2V2.4	13	P2R1V1.1	20	P2R2V3.2
2	P1R1V3.2	9	P1R2V4.8	14	P2R1V3.2	21	P2R2V4.0
3	P1R1V3.4	10	P1R2V10.4	15	P2R1V8.8	22	P2R2V10.9
4	P1R1V10.5	11	P1R2V23.0	16	P2R1V14.0	23	P2R2V21.5
5	P1R1V21.3	12	P1R2V28.2	17	P2R1V17.0	24	P2R2V27.3
6	P1R1V28.6			18	P2R1V21.2		
7	P1R1V29.1			19	P2R1V25.6		

Table 3 Mean velocity, direction and error RMS of the airspeed for P1R1 cases

Symbol	Mean (ASR)		Mean (AS)		Error Diff. (Upper) RMS (Lower)		
	V_W [m/s]	ψ_W [°]	V_W [m/s]	ψ_W [°]	V_W [m/s]	V_W [%]	ψ_W [°]
P1R1V1.4	0.448	– 44.8	1.36	77.4	– 0.912		– 122
					1.01	74.0	84.4
P1R1V3.2	3.96	31.3	3.21	– 12.8	0.750		44.1
					1.04	32.6	44.5
P1R1V3.4	4.71	50.6	3.39	19.1	1.32		31.5
					1.37	40.6	31.8
P1R1V10.5	10.4	31.2	10.5	1.89	– 0.100		29.3
					0.327	3.13	29.5
P1R1V21.3	20.3	36.7	21.3	3.20	– 1.00		33.5
					1.04	4.88	33.5
P1R1V28.6	26.4	35.5	28.6	– 3.55	– 2.20		39.1
					2.20	7.71	39.0
P1R1V29.1	27.0	31.0	29.1	–6.98	–2.10		38.0
					2.16	7.41	38.0

Table 4 Mean velocity, direction and error RMS of the airspeed for P1R2 cases

Symbol	Mean (ASR)		Mean (AS)		Error Diff. (Upper) RMS (Lower)		
	V_W [m/s]	ψ_W [°]	V_W [m/s]	ψ_W [°]	V_W [m/s]	V_W [%]	ψ_W [°]
P1R2V2.4	2.71	3.75	2.43	– 49.5	0.280		53.3
					0.926	38.2	58.6
P1R2V4.8	5.81	21.8	4.78	– 15.8	1.03		37.6
					1.08	22.8	37.8
P1R2V10.4	10.4	30.0	10.4	– 1.04	0.00		31.0
					0.353	33.9	31.0
P1R2V23.0	21.2	33.8	23.0	– 3.48	– 1.80		37.3
					1.84	8.02	37.3
P1R2V28.2	26.5	38.8	28.2	– 0.945	– 1.70		39.7
					1.83	6.48	39.7

and the dotted line (W+G) represents the airspeed calculated from the sum of two speeds: the wind speed measured by the weather meter at the flight test field and the ground speed from the GNSS receiver on the helicopter. The distance between the helicopter and the weather meter ranged approximately from 30–50 m. For clarity in visualization, the ψ_W value of the rotational airspeed sensor (ASR) in Figs. 13, 14, 15, 16 is adjusted by subtracting 30° from the original data.

The accuracy comparison between the two probes (P1 and P2) reveals that at low speeds (Figs. 10 and 11), there is negligible difference in performance between them; however, at velocities exceeding 5 m/s, the Pitot-type probe (P1) generally outperforms the cylindrical probe (P2), with the latter exhibiting larger errors. When assessing the impact of two different main rotor speeds (R1 and R2), the discrepancy between P1R1 and P1R2 using the Pitot-type probe (P1) is minimal. Conversely,

Table 5 Mean velocity, direction and error RMS of the airspeed for P2R1 cases

Symbol	Mean (ASR)		Mean (AS)		Error Diff. (Upper) RMS (Lower)		
	V_W [m/s]	ψ_W [°]	V_W [m/s]	ψ_W [°]	V_W [m/s]	V_W [%]	ψ_W [°]
P2R1V1.1	2.16	28.7	1.13	64.1	1.03		−35.4
					1.14	101	69.4
P2R1V3.2	3.06	−9.82	3.18	− 19.6	− 0.120		9.78
					0.457	14.4	12.4
P2R1V8.8	6.58	17.1	8.80	− 7.07	− 2.22		24.2
					2.27	25.8	24.1
P2R1V14.0	11.3	28.0	14.0	− 0.363	− 2.70		28.4
					2.75	19.6	28.4
P2R1V17.0	14.1	33.7	17.0	3.57	− 2.90		30.1
					3.00	17.6	30.1
P2R1V21.2	17.7	31.2	21.2	1.18	− 3.50		30.0
					3.48	16.4	30.1
P2R1V25.6	22.5	33.3	25.6	0.463	− 3.10		32.8
					3.08	12.1	32.9

Table 6 Mean velocity, direction and error RMS of the airspeed for P2R2 cases

Symbol	Mean (ASR)		Mean (AS)		Error Diff. (Upper) RMS (Lower)		
	V_W [m/s]	ψ_W [°]	V_W [m/s]	ψ_W [°]	V_W [m/s]	V_W [%]	ψ_W [°]
P2R2V3.2	3.22	7.53	3.22	2.32	0.00		5.21
					0.466	14.5	11.2
P2R2V4.0	3.08	−10.5	3.97	− 18.1	− 0.890		7.60
					1.30	32.9	17.3
P2R2V10.9	8.07	31.7	10.9	6.13	− 2.83		25.6
					2.85	26.2	25.7
P2R2V21.5	16.8	32.6	21.5	5.79	− 4.70		26.8
					4.77	21.1	26.9
P2R2V27.3	23.9	34.7	27.3	1.26	− 3.40		33.4
					3.47	12.7	33.4

for the cylindrical probe (P2), errors are more pronounced at higher rotational speeds (P2R2) compared to lower speeds (P2R1). The placement of the reference airspeed sensor below the main rotor requires a forward flight speed of at least 4.5 m/s to ensure the sensor moves beyond the downwash of the rotor. This requirement is based on the geometrical relative position between the front tip of the main rotor and the reference airspeed sensor, assuming uniform downwash velocity as predicted by momentum theory. Furthermore, when the main rotor speeds are 151.8 rad/s (R1, 1450 min^{-1}) and 162.3 rad/s (R2, 1550 min^{-1}), the linear velocities at the 0.15 m radius, where the probe's pressure hole of the rotational airspeed sensor is located, are 22.8 m/s and 24.3 m/s, respectively. If the helicopter's flight speed exceeds these values, the probe moving counter to the

flight direction would enter the backflow region, which is the upper limit of the measurable range of the rotational airspeed sensor. Within the velocity range of 4.5–23 m/s (Figs. 10 and 11), the error associated with the Pitot-type probe (P1) remains below 2 m/s and under 10%, whereas the error for the cylindrical probe (P2) ranges from 2–5 m/s and exceeds 10%. The time-history responses illustrated in Figs. 15c–g and 16c–e indicate that the airspeed magnitude V_W (ASR) measured by the cylindrical probe (P2) is frequently lower than that of the reference airspeed sensor (AS), and the errors widen at higher rotational speeds (R2 over R1). This discrepancy can be attributed to a reduction in total pressure difference as the body of the cylinder impeded air flow and acted as a form of resistance. For context, the accuracy of the rotational low-airspeed sensor LORAS 1000, designed for large manned helicopters, was validated in [24], demonstrating an error of approximately 4 KTAS (i.e., 2.06 m/s) in the flight direction during horizontal flight, irrespective of flight speed. The auxiliary line B1 in Fig. 10 is introduced for error comparison. The error of the developed sensor is lower than that of the LORAS 1000 within the measurable speed range using the Pitot-type probe (P1), which confirmed its suitability as a tool for measuring static low-airspeed. Furthermore, the dynamic vibratory responses of the helicopter's attitudes were evaluated by flight simulations under the automatic control of hovering and 10 m/s forward cruise, which introduced pseudo-white noise in the velocity signals of all the axes as measurement errors of the developed sensor. Assuming an acceptable threshold where the 3σ of attitude vibration amplitude is within 10°, the RMS value of the pseudo-white noise is set at 0.9 m/s; the auxiliary line B2 in Fig. 10 indicates this threshold. The measurement error of the developed sensor marginally surpasses this benchmark (below 7 m/s). However, given the considerably low accuracy of the reference sensor (AS) below 4.5 m/s, future research should focus on conducting online flight control experiments with the developed sensor to thoroughly assess its dynamic accuracy.

The accuracy difference in the direction ψ_W is comparatively analyzed for airspeeds of 4.5 m/s and above (Fig. 12), because the directional accuracy of the reference airspeed sensor is compromised by downwash turbulence below 4.5 m/s. Irrespective of probe type or rotational speed, an error of approximately 30±10° is observed; the angle of the rotational airspeed sensor has an offset of this value toward the direction of rotation. The sources of error are identified as follows: (1) The magnetometer detects the magnet passage occurs approximately 7° before the actual alignment with the magnet, (2) a delay from the differential pressure sensor (1 ms as per the datasheet, resulting in an angle error of ~9°), and (3) the transmission delay of pressure within the tube (1 ms, considering the speed of sound at 340 m/s and a total tube length per probe of 0.3 m, leading to an angle error of approximately 9°). When comparing the RMS error values of ψ_W between P1R1V10.5 (Table 3) and P1R2V10.4 (Table 4) –scenarios with nearly identical airspeeds and probes but varying main rotor speeds– the error differential is $31.0 - 29.5 = 1.5°$. The average rotational speeds for the main rotor were 150.3 and 160.5 rad/s, respectively. Therefore, the total processing delay can be evaluated as follows:

$$\frac{1.5 \times \pi/180}{160.5 - 150.3} \times 1000 = 2.6\,\text{ms} \tag{10}$$

which includes the differential pressure sensor delay and the pressure transmission delay inside the tubes, adding to 2 ms. Moreover, there is a 0.6 ms delay unaccounted for by these factors, corresponding to an ψ_W error of 5°. The aggregate of these delays aligns with an overall error of 30°, which closely approximates the findings presented in Fig. 12.

Although the Pitot-type probe is expected to exhibit a shorter delay due to the forward positioning of its total pressure hole on the arm, the actual delay observed with the Pitot-type probe is paradoxically increased. For the cylindrical probe, the variance in error because of fluctuations in the speed of the main rotor remains ambiguous. Nonetheless, calibration of the angle is deemed feasible, given the clear association of error with probe shape, main rotor velocity, and flight speed.

The cross-coupling error of the previously documented LORAS 1000, as detailed in [24], is approximately 3 KTAS, or 1.54 m/s, during horizontal flight, which is independent of the flight speed. For comparative analysis, auxiliary line B1 in Fig. 12 incorporates a 30-degree offset to compare this error. The error exhibited by the developed sensor is lower than that of its predecessor up to 21 m/s, approaching the upper limit of its measurable speed range. Consequently, the directional accuracy of the developed sensor is deemed sufficient, discounting the offset.

Moreover, even surpassing the aforementioned speed threshold does not precipitate abrupt escalations in errors for V_W and ψ_W (Figs. 10, 11, 12). Therefore, the developed rotational airspeed sensor in helicopter navigation and control would not detrimentally impact the system, even if flight speeds momentarily exceed the upper limit.

Time delay

The response delay for the velocity V_W was examined by calculating the correlation coefficient between the GNSS

Table 7 Results of time delay compared with the GNSS receiver

Flight cond.	P1R1	P1R2	P2R1	P2R2
Delay [s]	– 0.136	– 0.096	0.016	– 0.080

ground speed and V_W, adjusting the timing by 8 ms to identify the shift time at which the correlation coefficient peaked. This analysis considered data from three sequential flights involving acceleration, cruise, and deceleration phases, including data segments P1R1V21.3, P1R2V23.0, P2R1V21.2, and P2R2V21.5. The findings are summarized in Table 7, where positive values indicate a delay relative to the GNSS receiver, and negative values suggest advancement. With the exception of P2R1, which lagged behind of the GNSS receiver's ground speed, all other configurations advanced ahead. The GNSS receiver's ground speed, as utilized in the flight tests, exhibits a delay of approximately 0.2 s when compared to inertial navigation systems assessed by the authors, rendering even the delay of P2R1 negligible. Given that this GNSS receiver has been employed in the flight control systems of the developed helicopters, the time delay associated with the developed rotational airspeed sensor is unlikely to pose issues if its airspeed readings are integrated as control variables. Nonetheless, with the calculation of V_W and ψ_W conducted offline in this instance, future research will necessitate the development of online calculation strategies to minimize computational delays.

Conclusion

This study details the creation of a two-dimensional rotational low-airspeed sensor designed to measure airspeed in low-speed flight conditions of small helicopters, alongside the outcomes of flight tests conducted with a reference airspeed sensor for performance evaluation.

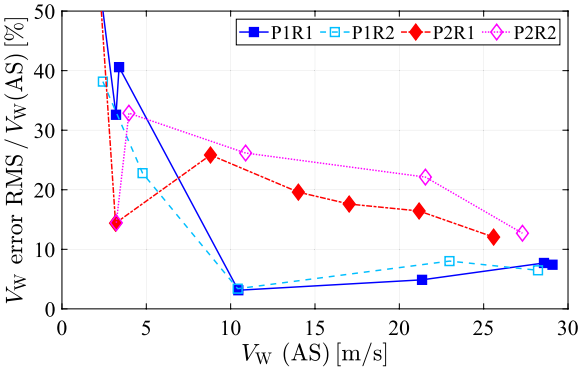

Fig. 11 Velocity error percentages with respect to probe types, rotational speeds and reference velocities

The developed sensor demonstrated promising results, especially with the Pitot-type probe, which consistently showed an error margin of 2 m/s or less across various flight and main rotor speeds, and less than 10% error at flight speeds exceeding 10 m/s. Despite the sensor's exposure to the flow field generated by the main rotor, no significant obstruction of external airflow or reduction in measured airspeed was observed. Conversely, cylindrical probes frequently registered lower airspeeds than the reference sensor, particularly at higher rotational speeds, attributed to reduced pressure differences due to inadequate airflow, with the cylinder acting as a barrier. Therefore, for small helicopters, the sensor configuration utilizing total pressure probes presents a clear advantage over traditional methods employing cylindrical static pressure probes.

Regarding the direction of airspeed, an error of approximately 30±10° toward the rotation direction was noted for flight speeds of 4.5 m/s or higher, irrespective of the probe type or rotational speed. The Pitot-type probe incurred greater errors compared to the cylindrical probe, with errors escalating alongside

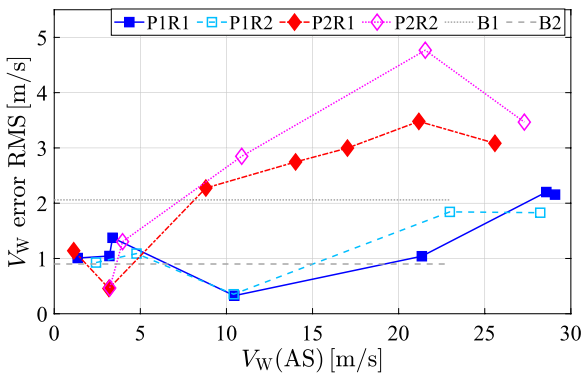

Fig. 10 Velocity error RMSs with respect to probe types, rotational speeds and reference velocities

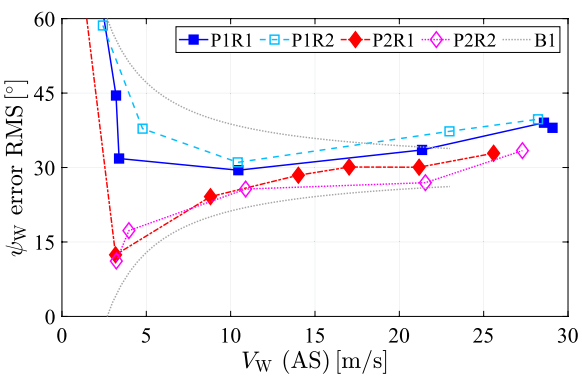

Fig. 12 Direction error RMSs with respect to probe types, rotational speeds and reference velocities

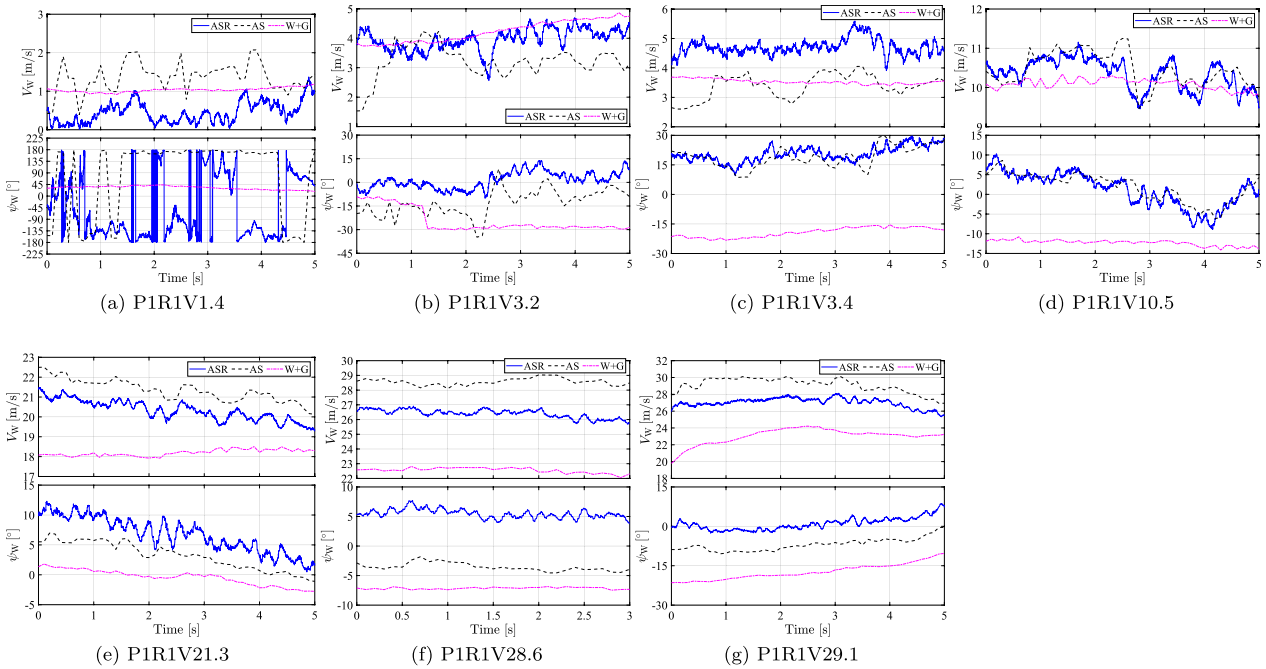

(a) P1R1V1.4 (b) P1R1V3.2 (c) P1R1V3.4 (d) P1R1V10.5

(e) P1R1V21.3 (f) P1R1V28.6 (g) P1R1V29.1

Fig. 13 Extracted time responses from flight test data: P1R1. The line denoted ASR in ψ_W is the value after subtracting 30 degrees

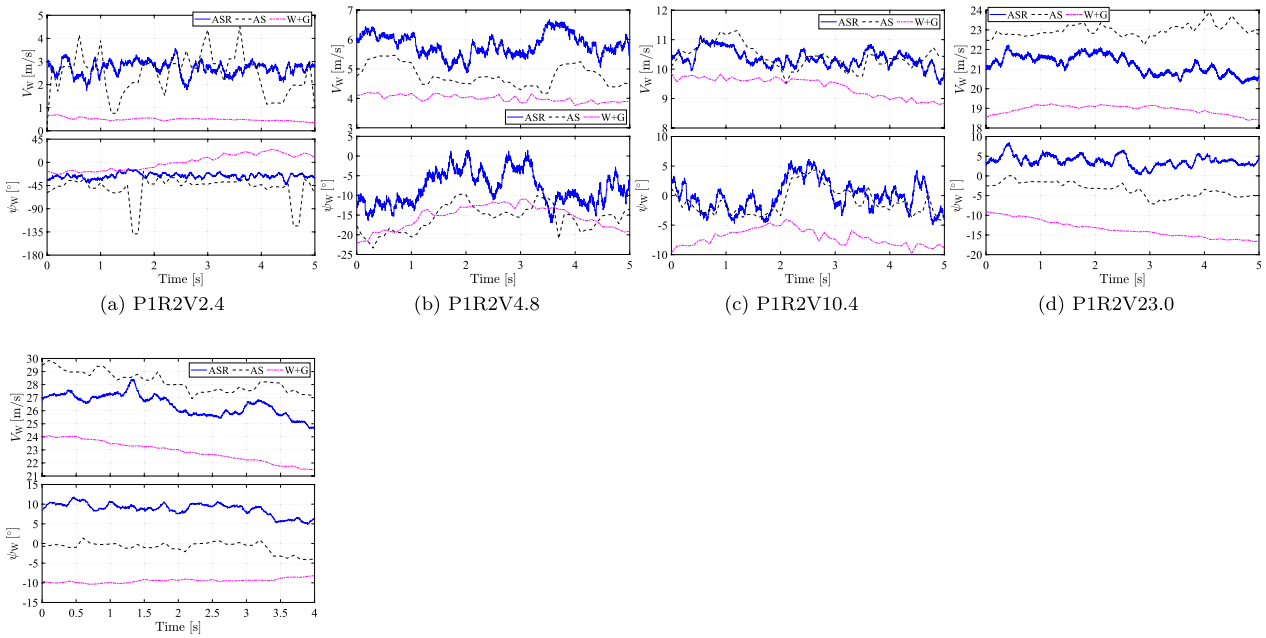

(a) P1R2V2.4 (b) P1R2V4.8 (c) P1R2V10.4 (d) P1R2V23.0

(e) P1R2V28.2

Fig. 14 Extracted time responses from flight test data: P1R2. The line denoted ASR in ψ_W is the value after subtracting 30 degrees

increases in rotational speed. Factors contributing to this discrepancy may include premature magnet detection by the magnetometer, inherent delays within the differential pressure sensor, and delays in pressure transmission within the tube. Nevertheless, calibration appears feasible due to the identifiable and consistent relationship between error and variables such as probe design, main rotor velocity, and flight speed. By addressing the directional offset, the accuracy of the developed airspeed sensor has been aligned with that

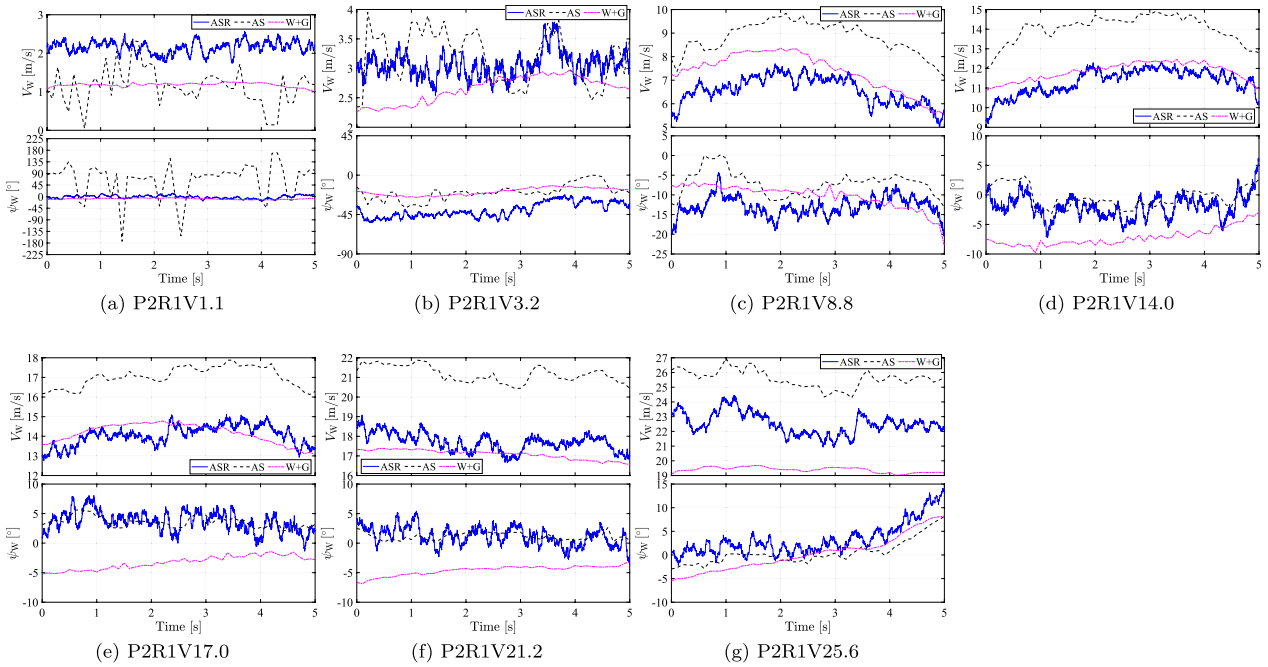

(a) P2R1V1.1 (b) P2R1V3.2 (c) P2R1V8.8 (d) P2R1V14.0

(e) P2R1V17.0 (f) P2R1V21.2 (g) P2R1V25.6

Fig. 15 Extracted time responses from flight test data: P2R1. The line denoted ASR in ψ_W is the value after subtracting 30 degrees

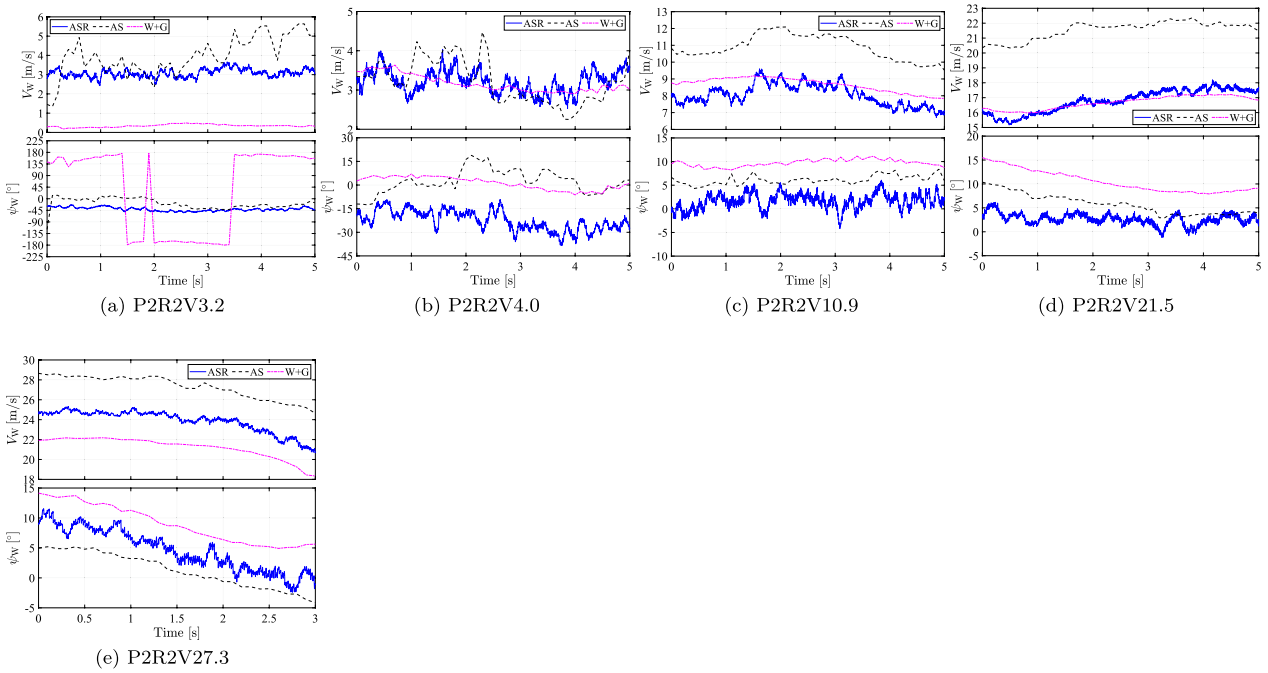

(a) P2R2V3.2 (b) P2R2V4.0 (c) P2R2V10.9 (d) P2R2V21.5

(e) P2R2V27.3

Fig. 16 Extracted time responses from flight test data: P2R2. The line denoted ASR in ψ_W is the value after subtracting 30 degrees

of traditional rotational sensors concerning both magnitude and direction.

The comparison of airspeed magnitude's time lag against GNSS receiver-measured speed data for navigation revealed that the time delay of the developed sensor was equal to or less than that of the GNSS receiver. In this study, airspeed calculations were performed offline based on differential pressure readings. With the development of an online calculation method characterized by minimal delay, the developed sensor holds potential as a

viable option for navigation or atmospheric disturbance detection.

Instances where the linear speed of the rotating probe surpassed the uniform wind speed beyond the measurable range of the sensor. However, even under these circumstances, the measured airspeed's magnitude and direction did not deteriorate abruptly. This observation suggests that navigation and control system issues could be mitigated, even at excessively high flight speeds.

Abbreviations

ADC	Air-data computer
AS	(Reference) Airspeed sensor
ASR	(Developed) Rotational airspeed sensor
GNSS	Global navigation satellite system
GPS	Global positioning system
IMU	Inertial measurement unit

Acknowledgements
Not applicable.

Author contributions
DF contributed to hardware/software development, flight tests, data analyses, and manuscript writing. TT contributed to the hardware design, manufacturing, and flight tests of the proposed sensor. All the authors have read and approved the final version of the manuscript.

Funding
Not applicable.

Availablility of data and materials
The datasets generated or analyzed during the current study are not publicly available because they apply for patents or export restrictions but are available from the corresponding author upon reasonable request.

Declarations

Competing interests
The authors declare that they have no competing interests.

Received: 10 July 2023 Accepted: 31 March 2024
Published online: 09 April 2024

References

1. Sakai N, Inagaki T (1988) Characteristics of a five-hole spherical pitot tube. Technical Report of National Aerospace Laboratory, Japan, TR-971
2. Laurence RJI, Argrow BM, Frew EW (2017) Wind tunnel results for a distributed flush airdata system. J Atmos Oceanic Tech 34(7):1519–1528. https://doi.org/10.1175/JTECH-D-16-0242.1
3. Matayoshi N, Okuno Y (2005) Flight test evaluation of ultrasonic velocimeter using research helicopter MuPAL-epsilon. JAXA Research and Development Memorandum, JAXA-RM-04-019
4. Kawahara R, Ogawara K, Shingin H (2017) Airspeed measurement using ultrasonic waves for micro UAVs. Trans JSME 86(887):19–00429. https://doi.org/10.1299/transjsme.19-00429. (**in Japanese**)
5. FT702LT datasheet, FT Technologies Ltd. (2018)
6. Shimura T, Inoue M, Tsujimoto H, Sasaki K, Iguchi M (2018) Estimation of wind vector profile using a hexarotor unmanned aerial vehicle and its application to meteorological observation up to 1000 m above surface. J Atmos Ocean Technol 35(8):1621–1631. https://doi.org/10.1175/JTECH-D-17-0186.1
7. Thielicke W, Hübert W, Müller U, Eggert M, Wilhelm P (2021) Towards accurate and practical drone-based wind measurements with an ultrasonic anemometer. Atmos Meas Tech 14(2):1303–1318. https://doi.org/10.5194/amt-14-1303-2021
8. Hrishikeshavan V, Yeo D, Chopra I (2015) Onboard flow sensing in a quad rotor biplane micro air vehicle for transition between hover and steady-level flight. Proceedings of the AHS Specialists Meeting on Unmanned Rotorcraft and Network Centric Operations
9. Yeo DW, Sydney N, Paley DA (2015) Onboard flow sensing for downwash detection and avoidance on small quadrotor helicopters. Proceedings of the AIAA Guidance, Navigation, and Control Conference, AIAA-2015-1769
10. Haneda K, Matsudaira K, Takahashi H (2023) Neural network-based airflow vector sensor using multiple MEMS differential pressure sensors. IEEE Access 11:40978–40987. https://doi.org/10.1109/ACCESS.2023.3270306
11. Zhao Z, Pan Y, Zhao R, Du L, Fang Z, Wu H, Niu X (2018) Design of a wind sensor based on cylinder diametrical pressure differences for boundary layer meteorological observation. MDPI Proc 2(13):1511. https://doi.org/10.3390/proceedings2131511
12. Matayoshi N, Hozumi K, Inokuchi H, Okuno Y (2003) Airdata sensor calibration flight test of NAL's research helicopter MuPAL-epsilon. Technical Memorandum of National Aerospace Laboratory, Japan, 779
13. IS 03-004 air data system datasheet, Marconi Avionics Limited
14. Kaletka J (1981) Evaluation of the helicopter low airspeed system LASSIE. Seventh european rotorcraft and powered lift aircraft forum, No.59
15. Helicopter air data system (HADS) datasheet, Meggitt Avionics (2011)
16. Bruschi P, Dei M, Piotto M (2009) A low-power 2-D wind sensor based on integrated flow meters. IEEE Sens J 9(12):1688–1696. https://doi.org/10.1109/JSEN.2009.2030652
17. Piotto M, Pennelli G, Bruschi P (2011) Fabrication and characterization of a directional anemometer based on a single chip MEMS flow sensor. Microelectron Eng 88(8):2214–2217. https://doi.org/10.1016/j.mee.2010.11.009
18. Bruschi P, Piotto M, Dell'Agnello F, Warec J, Roy N (2016) Wind speed and direction detection by means of solid-state anemometers embedded on small quadcopters. Proc Eng 168:802–805. https://doi.org/10.1016/j.proeng.2016.11.274
19. Wang Z, Qu J, Morin P (2023) Airflow-based odometry for MAVs using thermal anemometers. Int J Micro Air Vehicles. https://doi.org/10.1177/17568293221148385
20. Abichandani P, Lobo D, Ford G, Bucci D, Kam M (2020) Wind measurement and simulation techniques in multi-rotor small unmanned aerial vehicles. IEEE Access 8:54910–54927. https://doi.org/10.1109/ACCESS.2020.2977693
21. Duncan RE (1981) Low-range airspeed sensors. Thesis of the US Naval Postgraduate School, Accession No. ADA096359
22. Daw DF (1967) Helicopter airspeed indicator. US patent No. 3332282
23. Slabinski RJ, Filipkowski RC (1997) Multi-parameter air data sensing technique. US patent No. 5610845
24. Abbott WY, Boirun BH, Hill GE, Tavares EJ (1997) Flight evaluation Pacer Systems lowrange airspeed system LORAS 1000 final report. US Army Aviation Engineering Flight Activity, Accession No. ADA045222
25. Onksen PJ, Hundley RG, Hundley F (1982) Omnidirectional airspeed system. US patent No. 4360888

Publisher's Note